The Observed North Atlantic Meridional Overturning Circulation: Its Meridional Coherence and Ocean Bottom Pressure

SHANE ELIPOT

National Oceanography Centre, Liverpool, United Kingdom

ELEANOR FRAJKA-WILLIAMS

National Oceanography Centre, University of Southampton, Southampton, United Kingdom

CHRIS W. HUGHES

National Oceanography Centre, Liverpool, United Kingdom

JOSH K. WILLIS

Jet Propulsion Laboratory, California Institute of Technology, Pasadena, California

(Manuscript received 24 January 2013, in final form 20 November 2013)

ABSTRACT

Analyses of meridional transport time series from the Rapid Climate Change–Meridional Overturning Circulation (RAPID MOC) array at 26°N and from Argo float and altimetry data at 41°N reveal that, at semiannual and longer time scales, the contribution from the western boundary dominates the variability of the North Atlantic meridional overturning circulation (MOC), defined as the transport in the upper 1000 m of the ocean. Because the variability of the western boundary contribution is associated with a geostrophic overturning, it is reflected in independent estimates of transports from gradient of ocean bottom pressure (OBP) relative to and below 1000 m on the continental slope of the western boundary at three nominal latitudes (26°, 39°, and 42.5°N). Time series of western meridional transports relative to and below 1000 m derived from the OBP gradient, or equivalently derived from the transport shear profile, exhibit approximately the same phase relationship between 26° and 39°–42.5°N as the western contribution to the geostrophic MOC time series do: the western geostrophic MOC at 41°N precedes the MOC at 26°N by approximately a quarter of an annual cycle, resulting in a zero correlation at this time scale. This study therefore demonstrates how OBP gradients on basin boundaries can be used to monitor the MOC and its meridional coherence.

1. Introduction

At 26°N in the Atlantic Ocean, the Rapid Climate Change–Meridional Overturning Circulation and Heat-flux Array (RAPID–MOCHA, hereafter RAPID MOC array) has been in place since 2004 to monitor the variability of the meridional overturning circulation (MOC) and its heat flux with full-depth continuous measurements (Rayner et al. 2011). The array captures a circulation that consists of a relatively warm northward flow above approximately 1000 m, compensated between that depth and about 5000 m by a colder southward return flow. Because of this overturning nature, other observational arrays in the North Atlantic Ocean focus on monitoring only the deep return branch of the MOC that is expected to be concentrated on the western boundary (Stommel 1958), as a relatively strong deep western boundary current (DWBC) (e.g., Johns et al. 2008; Toole et al. 2011; Meinen et al. 2012). This is specifically the approach taken for the Meridional Overturning Experiment (MOVE) array since 2000 near 16°N in the North Atlantic (Send et al. 2011, and references therein), where only the returning southward flow in the western half of

Corresponding author address: Shane Elipot, Rosenstiel School of Marine and Atmospheric Science, University of Miami, 4600 Rickenbacker Causeway, Miami, FL 33149.
E-mail: selipot@rsmas.miami.edu

DOI: 10.1175/JPO-D-13-026.1

© 2014 American Meteorological Society

the basin is measured by density moorings, direct velocity measurements, and bottom pressure recorders (BPR). Furthermore, the western boundary is expected to constitute the primary pathway for propagating disturbances triggered by deep water formation anomalies at high latitudes. These anomalies travel first through coastally trapped waves (Johnson and Marshall 2002; Huthnance 1978; Elipot et al. 2013) and eventually through advection, as observed in models and in the ocean (e.g., Zhang 2010; van Sebille et al. 2011).

Yet, the same models and deep Lagrangian observations suggest that the DWBC is discontinuous and that interior pathways and recirculations are also important (Bower et al. 2009, and references therein), especially at the interface between the subpolar and subtropical gyres. It is therefore suggested that those so-called interior pathways also need to be monitored if one hopes to capture the water mass changes and adjustments of transports characterizing the Atlantic MOC. To monitor the return branch of the MOC in the real ocean, Hughes et al. (2013) propose to overcome the difficulty of multiple pathways by monitoring ocean bottom pressure (OBP) on basin boundaries. According to geostrophy, the difference between OBP on the eastern boundary and on the western boundary provides the zonally integrated geostrophic meridional transport. Consequently, the vertical gradient of boundary OBP differences determines the shear of the zonally integrated meridional transport and hence an overturning. Bingham and Hughes (2008) tested this concept successfully in an ocean global circulation model (OGCM) by comparing transports computed directly from velocities and from boundary OBP differences. They found that the contribution from the western boundary OBP dominated the total variance of the MOC at interannual time scales.

This paper tests whether OBP gradients measured in the real ocean, on the western boundary below 1000-m depth, capture the MOC. The references so far for the strength of the MOC are the time series from RAPID MOC array at 26°N (Kanzow et al. 2010; McCarthy et al. 2012) and the analysis of Argo and altimetry data near 41°N by Willis (2010). Specifically, are the deep southward western boundary transports derived from OBP gradients correlated with the MOC time series, and if yes, on which time scales? If yes, then this would demonstrate that OBP can be used to monitor the MOC in the North Atlantic.

This paper is organized as follows: Section 2 reviews the concepts that link zonally integrated meridional transports and OBP gradients on boundaries. The two equations that are considered define a western contribution and an eastern contribution to a total meridional transport. Section 3 applies the methodology of Elipot et al. (2013) and Hughes et al. (2013) at 26°N to derive the western boundary contribution to the geostrophic meridional transport between 1000- and 4000-m depths, relative to 1000 m. This transport is compared in detail to the MOC and its components. Section 4 focuses on similar time series: the two time series of OBP-derived western transport relative to and below 1000 m from Elipot et al. (2013) at 39° and 42.5°N and the upper-ocean geostrophic transport of Willis (2010) at 41°N. Section 5 compares the variability of the MOC time series and of the OBP-derived transport time series in order to study the meridional coherence of the MOC. It is found that the geostrophic MOC at 26° and 41°N, as well as the two deep western transport time series from Elipot et al. (2013) and the newly derived deep western transport at 26°N, are not correlated but rather are in quadrature (that is 90° out of phase) at time scales for which they are coherent. Section 6 provides a summary and concluding remarks.

2. On measuring zonally integrated meridional transports

The estimation of geostrophic meridional overturning transports is commonly based on the zonal thermal wind equation $f\partial(\rho v)/\partial z = -g\partial\rho/\partial x$ with f the Coriolis parameter, ρ the in situ density, v the meridional velocity, g the gravity, and z and x the vertical and zonal coordinates, respectively. Integrating across a zonal oceanic section delimited by vertical boundaries at longitude x_E on the east and at longitude x_W on the west gives

$$f\frac{\partial M(z)}{\partial z} = -g[\rho_E(z) - \rho_W(z)], \tag{1}$$

where $M(z) = \int_{x_W}^{x_E} \rho v\, dx$ is the meridional mass transport per unit depth. From (1) it is possible to define two terms: a western contribution to the overturning mass transport $\partial M_W/\partial z = g\rho_W/f$ arising from the density profile on the west $\rho_W(z)$ and an eastern contribution to the overturning mass transport $\partial M_E/\partial z = -g\rho_E(z)/f$ from the density profile on the east $\rho_E(z)$ (Hughes et al. 2013). While the partitioning of the time mean transport between east and west is arbitrary, time-dependent changes in the zonal integral are unambiguously associated with density changes on eastern and western boundaries.

At 41°N in the North Atlantic Ocean (Fig. 1), Willis (2010) estimated the right-hand side (rhs) of (1) from the combination of Argo floats and satellite altimetry sea surface height data (Willis and Fu 2008). He derived monthly time series of the two vertical density profiles from the surface down to the 2000-m isobaths on the east

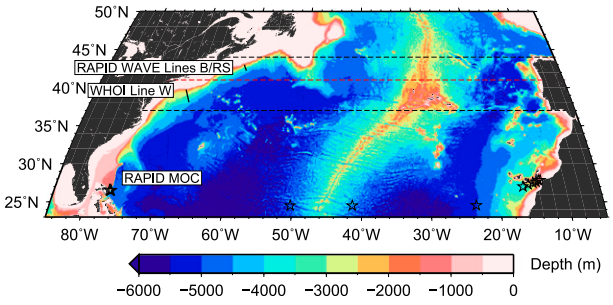

FIG. 1. Bathymetry of the Atlantic Ocean between 23° and 50°N from the Smith and Sandwell (1997) topography database, version 13.1. The two black segments indicate RAPID WAVE Lines B/Rapid-Scotian (B/RS) (42.5°N) and the WHOI Line W (39°N). The stars near 26°N indicate the locations of the moorings of the RAPID MOC array used to calculate the interior transport for the first year of deployment. The black dashed lines indicate the range of lat 37°–44°N within which the geostrophic transport from Argo is computed in this study, and the red dashed line indicates the lat of the Willis (2010) MOC estimate at 41°N.

and west boundaries at that latitude. The resulting sheared or baroclinic transport was referenced to a level of known motion at 1000 db, derived from the mapped geostrophic velocity of Argo floats at that level. The upper-ocean geostrophic transport was then obtained by integrating from the surface to the average zero-crossing depth of the transport profile, 1130 m at that latitude. By adding an estimate of the Ekman transport from the National Centers for Environmental Prediction (NCEP) reanalyses' wind stress, Willis (2010) reported a time series of the MOC near 41°N. The updates of these time series are plotted in Fig. 2b.

The RAPID MOC array also uses (1) to obtain the unreferenced interior geostrophic component of the total meridional transport at that latitude, though the eastern and western boundaries are not strictly vertical (Rayner et al. 2011). The density profile on the west is measured by combining a tall dynamic height mooring (WB2) spanning from the surface down to 3800 m, 20 km east of Abaco, Bahamas, and the near-bottom data from two other moorings along the base of the continental slope down to 4800 m and out to 45 km east of the Bahamas [see Fig. 3 of this paper and Figs. 4 and 5 in Rayner et al. (2011)]. The eastern boundary density profile is not vertical either but obtained from a stack of moorings crawling up the African continental slope across a horizontal distance of more than 1100 km. In the use of (1), the intervening topography of the Mid-Atlantic Ridge (MAR) is taken into account by measuring intermediate density profiles on both sides and using this information below 3700 m (the maximum depth at which the MAR is permeable to east–west exchanges of water masses). The interior geostrophic transport is augmented by a volume transport estimated from velocity measurements between mooring WB2 and Abaco in order to form an unreferenced midocean transport (Johns et al. 2008). When this last transport is added to an Ekman transport calculated from wind stress data, and the Gulf Stream transport from induced voltages on telephone cables across the Florida Strait (Baringer and Larsen 2001), the top-to-bottom transport shear is obtained. A zero net total mass transport constraint is imposed to reference the midocean transport and obtain the overall profile of volume transport per unit depth. The reader is referred to Rayner et al. (2011) for a detailed description of the RAPID MOC array and to Kanzow et al. (2010) for the methodology.

The strength of the MOC at each available time step can be defined as the maximum of the meridional overturning streamfunction: $\Psi^{\mathrm{MAX}}(t) = \int_{-h_{zc}(t)}^{0} Q(z,t)\,dz$, where $h_{zc}(t)$ is the time-dependent maximizing depth of this integral, and the depth of the first zero crossing of $Q(z, t)$, which is the volume transport per unit depth (Kanzow et al. 2010). An update of the MOC time series with about 7 years of data is plotted in Fig. 2d. In the rest of the text the time dependency is implicit and the t notation is omitted.

An alternative to (1) exists by either zonally integrating the zonal geostrophic balance equation or (in the case of vertical sidewall only) using the hydrostatic relation $-\partial p/\partial z = \rho g$ to substitute pressure for density:

$$f\frac{\partial M(z)}{\partial z} = -\frac{\partial p_W(z)}{\partial z} + \frac{\partial p_E(z)}{\partial z}. \qquad (2)$$

This equation defines two transport shears or overturnings by the vertical gradients of OBP on the western and the eastern boundaries. In contrast to (1), (2) says nothing about the location of the boundaries with depth: it does not formally require the boundaries to be vertical. It allows the overturning transport to be evaluated exactly between the physical boundaries of the basin, provided that the pressure gradient can be measured with sufficient resolution along these boundaries. Hughes et al. (2013) describe a methodology to apply this equation to ocean data. Bingham and Hughes (2008) found the application of this equation to be successful in an OGCM at 42°N in the North Atlantic Ocean. In fact, they found that the first term on the rhs of (2) was sufficient to explain more than 90% of the variance of meridional transports at interannual time scales, showing the predominance of the western boundary for the variance of the MOC in their model.

In turn, Elipot et al. (2013) used in situ data to estimate the first term on the rhs of (2) at two latitudes in the

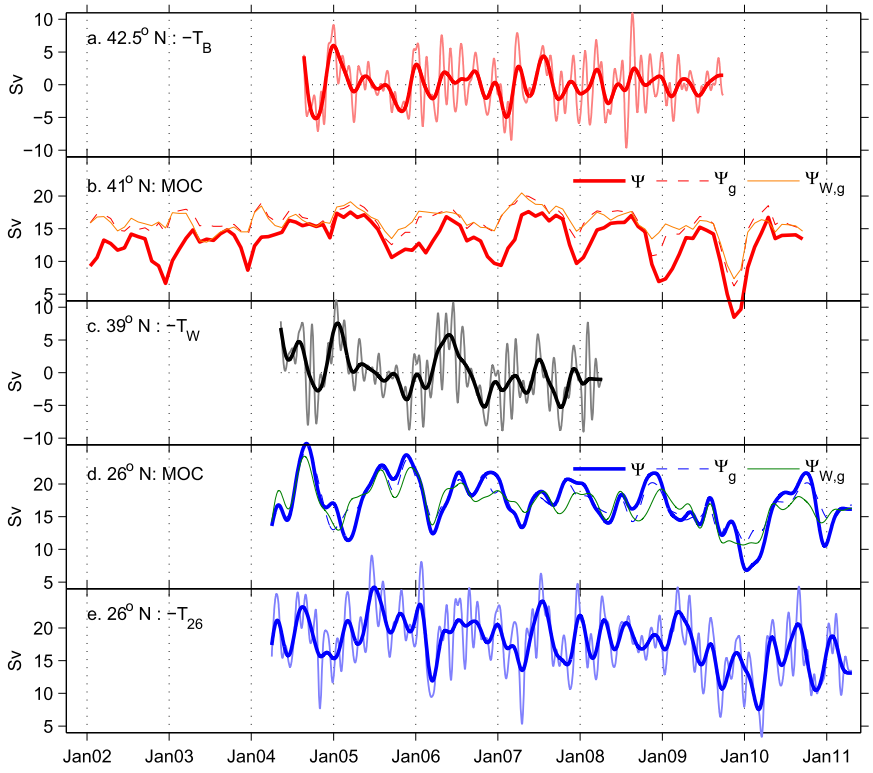

FIG. 2. Overturning transport time series used in this study. MOC time series at (d) 26°N and (b) 41°N. The term Ψ is the total MOC (geostrophic plus Ekman), Ψ_g is the geostrophic contribution, and $\Psi_{W,g}$ is the western boundary geostrophic contribution (see text). Monthly (light curves) and 3-monthly (heavy curves) low-pass-filtered time series of western boundary meridional transport T between 1000 and 4000 m referenced to 1000 m from (a) RAPID WAVE Line B/RS T_B, from (c) WHOI Line W T_W, and from (e) RAPID MOC T_{26}.

North Atlantic. They derived the western boundary contribution to the zonally integrated meridional volume transport, relative to and below 1000 m, down to 4000-m depth. They used estimates of OBP gradient from BPR at Line B of the RAPID Western Atlantic Variability Experiment (WAVE) deployed on the continental slope of the western boundary near 42.5°N (Fig. 1). The resulting time series has the caveat of not being reliable on time scales longer than about a year because of unavoidable instrumental drifts of BPRs (Polster et al. 2009), and unfortunately this limitation applies here too. To circumvent this issue, Hughes et al. (2013) introduced a drift-free method to derive OBP gradients along sloping boundaries using density and velocity data. Elipot et al. (2013) applied this method to derive a second time series of western transport relative to and below 1000 m at the Woods Hole Oceanographic Institution (WHOI) Line W mooring array near 39°N (Toole et al. 2011). These two OBP gradient-derived time series were analyzed to determine if the western boundary communicated pressure—and speculatively transport—anomalies, as expected from theories and numerical experiments (Johnson and Marshall 2002) and OGCM runs (Roussenov et al. 2008; Bingham et al. 2007). It was found that the two time series were coherent and in phase on time scales longer than 3 months, but also on shorter time scales with a phase slope that identified a propagating signal probably carried by coastally trapped

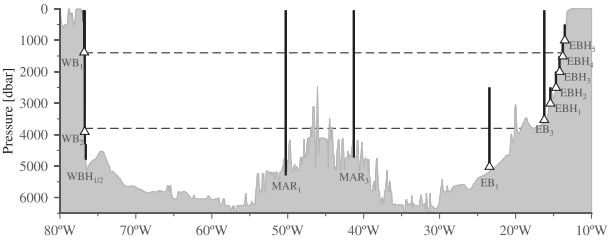

FIG. 3. A section of the topography along the path defined by the moorings of the RAPID MOC array for the first year of deployment shown in Fig. 1. The triangles indicate the BPR instruments used in this study to calculate the boundary pressure gradients on the western and eastern boundaries. The vertical lines represent the moorings of the array shown with stars in Fig. 1 that are used to calculate the interior transport (except mooring WB1). The horizontal dashed lines indicate the depth range over which the boundary pressure gradients are estimated from these BPRs.

waves rather than advected by the DWBC. The question is now are these time series of transports from the OBP gradient on only the western boundary representative of the North Atlantic MOC? Section 3 answers this question near 26°N and section 4 answers it near 41°N.

3. Western transport overturning at 26°N

The methodology of Hughes et al. (2013) in the framework of RAPID WAVE, applied by Elipot et al. (2013), was motivated by the expectation that the vertically integrated boundary OBP gradient was indicative of overturning processes of the North Atlantic MOC. This expectation is confirmed in this section in two steps at 26°N. First, we use transport profiles and independent BPR records for the first year of the RAPID MOC array to verify that the boundary pressure gradient is proportional to the vertical shear of the geostrophic transport profile, as predicted by (2). Second, in order to not be limited by only 1 year of available BPR data on the western boundary, we use about 7 years of RAPID MOC data to derive a time series of western contribution to the zonally integrated meridional transport relative to and below 1000 m. To understand which transport processes are associated with this new time series, it is studied with respect to the MOC, as well as the full transport profiles.

a. Western and eastern boundary pressure gradients

To verify that the OBP gradient is proportional to the transport shear, the two sides of (2) are compared for the first year of RAPID MOC. We actually compute a double vertical integration of (2) as

$$\underbrace{\int_{z_2}^{z_1}\left[-\int_{z}^{z_1}\frac{\partial Q'_{W,g}(\alpha)}{\partial\alpha}d\alpha\right]dz}_{\text{(i)}}+\underbrace{\int_{z_2}^{z_1}\left[-\int_{z}^{z_1}\frac{\partial Q'_{E,g}(\alpha)}{\partial\alpha}d\alpha\right]dz}_{\text{(ii)}}$$
$$=\underbrace{\frac{1}{\rho_0 f}\int_{z_2}^{z_1}\left[-\int_{z}^{z_1}-\frac{\partial p'_W(\alpha)}{\partial\alpha}d\alpha\right]dz}_{\text{(iii)}}$$
$$+\underbrace{\frac{1}{\rho_0 f}\int_{z_2}^{z_1}\left[-\int_{z}^{z_1}\frac{\partial p'_E(\alpha)}{\partial\alpha}d\alpha\right]dz}_{\text{(iv)}}, \tag{3}$$

where primes denote anomalies from a time mean. The computations are conducted in the depth range delimited by the bases of moorings WB1 and WB2 at $z_1 = 1382$ m and $z_2 = 3898$ m, respectively (Fig. 3).

On the left-hand side (lhs) of (3), $Q'_{W,g}(z)$ and $Q'_{E,g}(z)$ are the western and eastern contributions, respectively, to the geostrophic meridional volume transport anomaly per unit depth. These dynamical contributions are calculated following the methodologies of Kanzow et al. (2010) and Johns et al. (2011) that do not use BPR measurements. First, the geostrophic transport profile $Q_g(z)$ is obtained by setting the Ekman transport to its mean value for conducting the RAPID MOC calculations. The western geostrophic contribution $Q_{W,g}(z)$ is further obtained by replacing in the calculations the density profiles at the eastern boundary and on both sides of the MAR by their time means. The eastern boundary contribution $Q_{E,g}(z)$ is obtained by replacing the Florida Current (FC) transport, the transport west of mooring WB2, and the western and MAR density profiles by their time means. After removing their respective time means, each of the east or west geostrophic transport profiles is differentiated with respect to z to obtain the transport shears that are used to calculate terms (i) and (ii) in (3). For each term, the first integration is calculated by setting the transport per unit depth to zero at $z = z_1$, which is our reference level for this exercise.

The OBP gradient anomalies on the western boundary ($\partial p'_W/\partial z$) are calculated in one step from a BPR at WB1 (deployed for 1 year only in 2004–05) and a BPR at WB2. The OBP gradient anomalies on the eastern boundary ($\partial p'_E/\partial z$) are calculated in steps in the same depth range with the BPRs deployed on the continental slope from mooring EB3 at 3520 m to mooring EBH4 at 1558 m. OBP anomalies at the depths of WB2 and WB1 were extrapolating linearly from EB3 and EBH4, respectively (Fig. 3). Each BPR record was detided by least squares fitting 97 tidal components with periods of 28.0062 h (component 2Q1) and shorter. Obvious drifts acting on time scales longer than 50 days approximately remained in the residuals, with the most severe of the order of 70–80 mbar over 1 year at EB3 and EBH2. These drifts were removed, as far as possible, by the standard method of subtracting exponential–linear fits as in Polster et al. (2009). The time series of OBP relative to $z = z_1$ on the western and on the eastern boundaries are plotted in Fig. 4. The terms (iii) and (iv) on the rhs of (3) are computed by further integrating these curves.

The time series for all terms and the sum of each side of (3) are shown in Fig. 5a. We conduct cross-spectral analyses to determine how well the terms on the lhs of (3) represent the terms on the rhs. Comparisons between a pair of time series $[x(t), y(t)]$ are conducted by examining as a function of frequency ν the gain factor G_{xy} and coherence squared γ^2_{xy}:

$$G_{xy}(\nu)=\frac{|S_{xy}(\nu)|}{S_{xx}(\nu)} \quad \text{and} \quad \gamma^2_{xy}(\nu)=\frac{|S_{xy}(\nu)|^2}{S_{xx}(\nu)S_{yy}(\nu)}, \tag{4}$$

where $S_{xy}(\nu)$ is the power cross-spectrum between $x(t)$ and $y(t)$, and $S_{xx}(\nu)$ is the power autospectrum of $x(t)$.

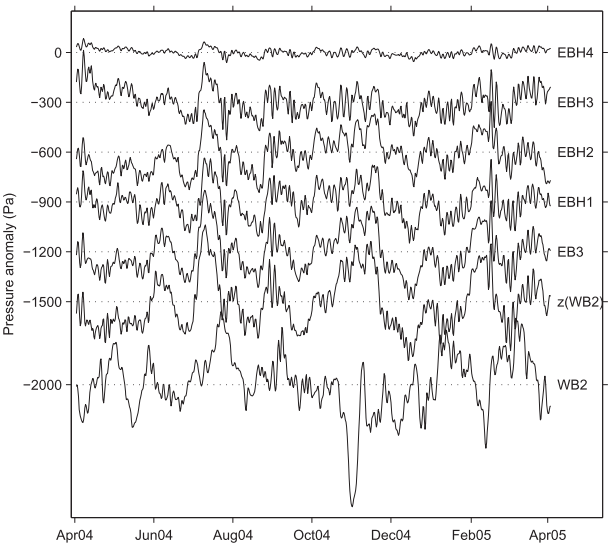

FIG. 4. Time series of ocean bottom pressure anomalies on the eastern boundary at moorings EBH4, EBH3, EBH2, EBH1, and EB3, and on the western boundary at mooring WB2. The curve labeled z(WB2) is the pressure anomaly time series on the eastern boundary at 3898 m, depth of mooring WB2, interpolated linearly with depth from the pressure anomaly time series at moorings EB3 and EB1 (see Fig. 3). These time series are obtained by integrating pressure gradients calculated from BPR records, relative to zero at 1382 m, the depth of mooring WB1. Arbitrary offsets to each curve, as indicated by the dotted lines, were added for plotting purpose.

When the phase of $S_{xy}(\nu)$ is near zero, $G_{xy}(\nu)$ can be thought as a regression coefficient of $y(t)$ onto $x(t)$, but as a function of frequency. Where $G_{xy}(\nu) < 1$ implies that $y(t)$ underestimates the variance of $x(t)$ at frequency ν. The term $\gamma^2_{xy}(\nu)$ measures how much of the variance of one variable can be explained by the other variable, irrespective of their relative magnitudes and phases. We analyze the results for time scales longer than 10 days, which is an approximate limit for the balance of the transport components at the RAPID MOC array (Kanzow et al. 2007). In Figs. 5b and 5c, estimates of $G_{xy}(\nu)$ and $\gamma^2_{xy}(\nu)$ are shown between western terms (i) and (iii), between eastern terms (ii) and (iv), between the totals (i) + (ii) and (iii) + (iv), and additionally between (i) + (ii) and (iii).

We find that the phase of S_{xy} between terms (ii) and (iv) (not shown) is different from zero; in contrast, the phases of S_{xy} for the other two pairs of the time series are near zero for all frequencies. For those pairs, we think of their gain factor as a regression coefficient of a profile-derived transport onto a pressure-derived transport. Figure 5c shows that the western contribution to the transport shear [term (i)] is very close the western boundary pressure gradient [term (iii)] as G_{xy} between these two terms is between 0.62 and 1.17. This is consistent with the fact that γ^2_{xy} between these two terms is always higher than 0.56, reaching 0.97 at the longest period (Fig. 5b). This result is remarkable considering that the pressure gradient on the western boundary is estimated from only two BPRs separated by 2510 m of depth. In contrast, the eastern contribution to the transport shear [term (ii)] badly underestimates the pressure gradient on the eastern boundary [term (iv)] with G_{xy} always less than 0.57, despite the fact that γ^2_{xy} is relatively high and coherent except marginally around the 50-day period. The reasons for this low G_{xy} but high γ^2_{xy} between terms (ii) and (iv) are not known. The severe drifts of the BPRs may not have been corrected sufficiently to accurately estimate the pressure gradient. We also speculate that it is because the density measurements on the east at RAPID MOC may not be sufficient to capture the full gradient of OBP because geostrophic flows over the sloping bottom can contribute to the boundary OBP gradient, an issue that becomes more important where the continental slope is less steep, as on this eastern boundary (Hughes et al. 2013). No velocity data are available for that time period to verify this conjecture. As a consequence, G_{xy} between the total transport shear [term (i) + (ii)] and the total pressure gradient [term (iii) + (iv)] is only on average 0.54 across frequencies. Finally, because the eastern contribution to the shear [term (ii)] is of relatively small magnitude, the total shear [term (i) + (ii)] is also very close to the western pressure gradient only [term (iii)] because G_{xy} is always larger than 0.6 (dashed line in Fig. 5c). The γ^2_{xy} between these two terms (dashed line in Fig. 5b) implies that term (i) + (ii) always explains more than 50% of the variance of term (iii) except near the 12-day period. This means that the OBP gradient between 1382 and 3898 m on only the western boundary represents relatively closely the total RAPID MOC meridional transport shear between these depths.

No more BPRs were deployed at WB1 after the first year of the array so we cannot test (2) at longer time scales, and our conclusions are strictly valid for intra-annual time scales. If more data were available, we would expect an increasing error because of drift corrections applied to BPR records that can also suppress the true signal variance (Hughes et al. 2013). However, the physics of (2) and the dominance of the western boundary should still hold at interannual time scales, as suggested by Bingham and Hughes (2008) in an OGCM for both the depth ranges of the upper and lower branches of the Atlantic MOC at 42°N.

The observational approach described in Hughes et al. (2013) and applied by Elipot et al. (2013) consists of estimating the OBP gradient relative to and below 1000 m in order to derive the meridional overturning transport according to (2). We are confident that we have demonstrated that the shear of the western geostrophic transport from RAPID MOC represents the western OBP

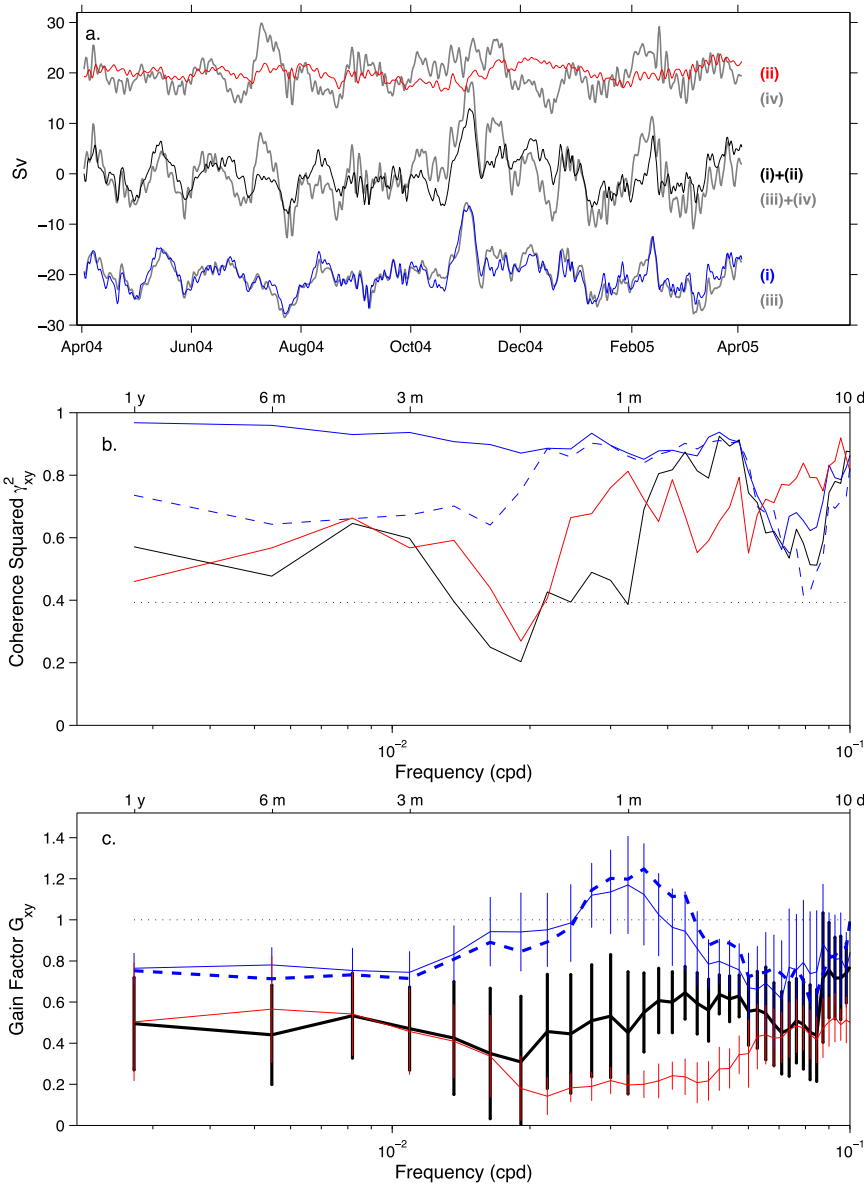

FIG. 5. (a) Volume transport anomalies between 1382 and 3892 m at the RAPID MOC array relative to 1382 m, calculated from boundary pressure records (gray curves) or from RAPID MOC geostrophic transport profiles (colored and black curves). The two lower curves (offset by −20 Sv) are the western boundary contributions, the two upper curves (offset by +20 Sv) are the eastern boundary contributions, and the two middle curves are the sum of the eastern and western contributions. The labels of the curves correspond to the terms in (3). (b) Coherence squared from term (i) to (iii) (solid blue), from term (ii) to (iv) (solid red), from term (i) + (ii) to (iii) + (iv) (solid black), and from term (i) + (ii) to (iii) (dashed blue). The horizontal dotted line is the formal 95% confidence level. (c) Gain factor from term (i) to (iii) (solid blue), from term (ii) to (iv) (solid red), from term (i) + (ii) to (iii) + (iv) (solid black), and from term (i) + (ii) to (iii) (dashed blue). For legibility this last curve is plotted without its error bars, which are of the same magnitudes as for the other curves. Error bars are approximated 95% confidence intervals computed following Bendat and Piersol (1986, p. 338).

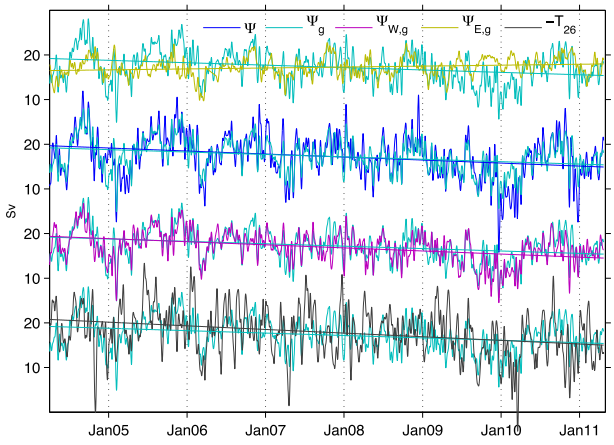

FIG. 6. MOC time series at 26°N from the RAPID MOC array: total MOC, MOC with Ekman transport variability removed (or geostrophic), western boundary geostrophic MOC, eastern boundary geostrophic MOC, and negative western boundary meridional transport $-T_{26}$ between 1000 and 4000 m referenced to 1000 m. The straight lines are the least squares fits to linear trends. Note the nonmonotonic labels of the y axis.

gradient between 1382 and 3898 m (or vice versa). As such, we make the assumption that the same shear transport profile also represents the OBP gradient between 1000 and 4000 m. We use this assumption in the rest of the paper to derive at 26°N a time series of western transport relative to and below 1000 m, integrated down to 4000 m. We study next whether this transport is representative of the MOC.

b. *Western overturning transport relative to and below 1000 m and its relationship to the MOC*

We compute the western geostrophic transport relative to 1000 m in the 1000–4000-m-depth layer as

$$T_{26} = \int_{-4k}^{-1k} \left[-\int_{z}^{-1k} \frac{\partial Q_{W,g}(\alpha)}{\partial \alpha} d\alpha \right] dz. \qquad (5)$$

With this convention, a negative value of T_{26} corresponds to a southward transport relative to 1000 m that we interpret as a strengthening of the MOC. For comparison, the negative of T_{26} is plotted in Fig. 6 besides the time series of the MOC and its contributions at 26°N (see below). In the rest of this section, we examine the relevance of T_{26} for the monitoring the MOC.

1) COMPARISON TO THE MOC AND ITS DYNAMICAL CONTRIBUTIONS

(i) MOC contributions

We define the MOC, or Ψ, as the integrated transport profile between the surface and 1000 m. For 10-day low-pass-filtered time series, Ψ differs very little from Ψ^{MAX} calculated as in Kanzow et al. (2010), which involves a time-varying lower limit of integration. Here, between Ψ and Ψ^{MAX}, the mean difference is −0.2 Sverdrups (Sv; $1\,\mathrm{Sv} \equiv 10^6\,\mathrm{m^3\,s^{-1}}$) and the rms difference is 0.4 Sv from 1 April 2004 to 23 April 2011. These differences are negligible for our purpose.

TABLE 1. Std dev $\sigma(X)$ in Sv of the 26°N MOC, its contribution, and of the negative of the T_{26} transport from 1 April 2004 to 23 April 2011. The std dev of the differences from Ψ are also listed. The std dev are listed for the 10-day and 6-month low-pass-filtered time series.

X	Ψ	Ψ_g	$\Psi_{W,g}$	$\Psi_{E,g}$	$-T_{26}$
$\sigma(X)_{10\text{-day}}$	4.9	3.6	3.5	2.1	5.4
$\sigma(\Psi - X)_{10\text{-day}}$	—	2.7	3.1	5.0	5.4
$\sigma(X)_{6\text{-month}}$	3.4	2.6	2.4	1.3	2.6
$\sigma(\Psi - X)_{6\text{-month}}$	—	1.3	1.8	3.3	2.5

The MOC is the sum of three components: the FC transport, the Ekman transport, and the upper-midocean transport (McCarthy et al. 2012). Here, we consider instead dynamical contributions to the MOC. Following Johns et al. (2011), we compute the geostrophic contribution Ψ_g from the transport profile $Q_g(z)$ obtained by setting the Ekman transport to its mean value, as described previously. Additionally, we compute the western geostrophic contribution $\Psi_{W,g}$ from $Q_{W,g}(z)$. The geostrophic contribution from the eastern boundary $\Psi_{E,g}$ is calculated conversely from $Q_{E,g}(z)$. These various contributions (shown in Fig. 6) are neither all independent nor additive for Ψ, yet we will show that they help to quantify the relative importance of the overturning processes, notably as a function of time scales considered. The standard deviations and rms differences from Ψ of the dynamical contributions to Ψ are listed in Table 1 for 10-day or 6-month low-pass-filtered time series. This table indicates that the variance of Ψ_g is significantly less than the variance of Ψ. While $\Psi_{W,g}$ exhibits almost as much variance as Ψ_g, the variance of $\Psi_{E,g}$ is much reduced compared to Ψ_g (more than 40% less variance).

We compare the variability of Ψ and its contributions by analyzing their spectra (Fig. 7) and analyzing their cospectra by considering their γ^2_{xy} and G_{xy} (Fig. 8). The peaks at periods near 6 months and 1 year in the Ψ spectrum seem attributable to $\Psi_{E,g}$, which is confirmed by γ^2_{xy} between them. This is consistent with the findings of Kanzow et al. (2010), who showed that the eastern boundary controlled the annual cycle of the MOC, likely via the midocean transport response to oscillating winds along the west coast of Africa (Chidichimo et al. 2010). Nevertheless, γ^2_{xy} between Ψ and $\Psi_{E,g}$ is rarely significant outside that frequency band, and their G_{xy} indicates that $\Psi_{E,g}$ makes a weak contribution to Ψ. In fact, near the 3.5-year period where Ψ and $\Psi_{E,g}$ are significantly

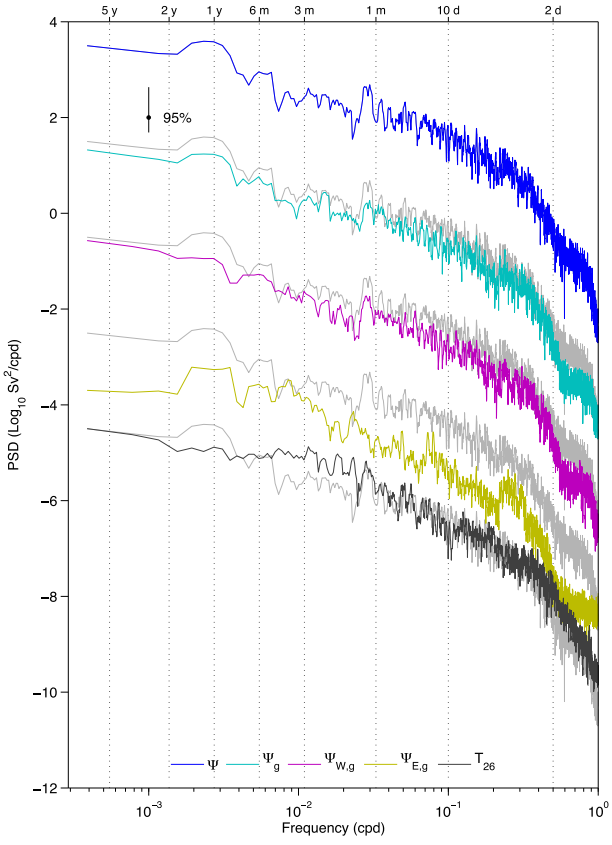

FIG. 7. Multitaper spectra of the time series of Fig. 6. Spectra were computed from demeaned but not detrended time series. The spectra are successively offset by 2 decades. The spectrum of Ψ is repeated as background gray curves for comparison. The 95% confidence interval indicated in the top left corner is calculated with a number of degrees of freedom equal to twice the number of tapers used for the spectral estimation. Spectra are estimated using a multitaper estimator with five Slepian tapers following Percival and Walden (1993).

coherent again, the phase of their cross-spectrum (not shown) is actually near 145°, indicating that $\Psi_{E,g}$ is anticorrelated with Ψ at these time scales. At periods just longer than 1 month, a peak in the Ψ spectrum appears related to $\Psi_{W,g}$. Elipot et al. (2013) noted a similar peak in the spectrum of the western boundary contribution to meridional transport below 1000 m derived from the WHOI Line W near 39°N (discussed in the next section), which they attributed to topographic waves or more generally coastally trapped waves propagating along the western boundary. Between Ψ and Ψ_g, γ^2_{xy} is not significant at periods shorter than 5 months, which suggests that the local Ekman overturning dominates the Ψ variance at these relatively high frequencies. In contrast, γ^2_{xy} is larger than 0.5 and significant for periods longer than 5 months, which in turn suggests that the geostrophic contribution dominates the variance at low frequencies. However, G_{xy} from Ψ_g to Ψ is less than 1 at low frequencies, which indicates that Ψ_g remains an underestimate of Ψ and suggests that an Ekman overturning pertains even at those frequencies. The γ^2_{xy} and G_{xy} between Ψ and $\Psi_{W,g}$ indicate that $\Psi_{W,g}$ often explains a dominant fraction of the variance of Ψ and is as good as, or better than, Ψ_g at explaining the variance of Ψ for periods longer than approximately 2 years.

In conclusion, despite the importance of the eastern boundary for near-annual frequencies, cross-spectral analyses show that the geostrophic component clearly dominates the variance of the MOC time scales longer than 6 months and that most of the geostrophic variance arises from the western boundary.

(ii) T_{26} comparison

We now compare T_{26} to Ψ and its contributions. The time mean of T_{26} is 17.9 Sv southward and almost equal to the time mean 17.3 Sv northward of Ψ. This is not surprising because in the mean the zero crossing of the transport profile is 1001 m and the mean southward transport below 4000 m is small for our time period of analysis. Table 2 lists correlations, hereafter noted r_{xy}, between $-T_{26}$ and the Ψ contributions. The transport $-T_{26}$ is significantly correlated with Ψ, with $r_{xy} = 0.44$ for the 10-day low-pass-filtered time series, but this implies that T_{26} accounts for only 19% of the variance of Ψ. The transport $-T_{26}$ is the most correlated with $\Psi_{W,g}$ ($r_{xy} = 0.58$) and is not correlated with $\Psi_{E,g}$. These correlations between $-T_{26}$ and the Ψ contributions actually depend on the filtering applied to the time series. This is first seen when the correlations are recalculated for the 6-month low-pass-filtered time series: in that case, $r_{xy} = 0.69$ with Ψ and $r_{xy} = 0.83$ with $\Psi_{W,g}$.

To better quantify the influence of the filtering, we calculate a new correlation coefficient between $-T_{26}$ and the Ψ contributions, which we denote $\rho_{xy}(\nu_c)$, where the time series are low-pass filtered with a frequency cutoff ν_c. To account for the increasing autocorrelation inherent to the time series and the filtering, we assess the significance of $\rho_{xy}(\nu_c)$ by the method of Ebisuzaki (1997) for serially autocorrelated time series. For each calculation of $\rho_{xy}(\nu_c)$ between a pair of time series we also calculate $\rho_{xy}(\nu_c)$ between a simulated pool of 1000 pairs of time series that have exactly the same autospectra as the original time series but for which the phases of the Fourier components as a function of frequency have been randomly assigned. The value of the 95th percentile of the distribution of the correlations calculated with the simulated time series is taken as our 95% confidence level.

Shown in Fig. 9, $\rho_{xy}(\nu_c)$ between $-T_{26}$ and the Ψ contributions are always positive and significant. The $\rho_{xy}(\nu_c)$ generally increase as the low-pass filter period

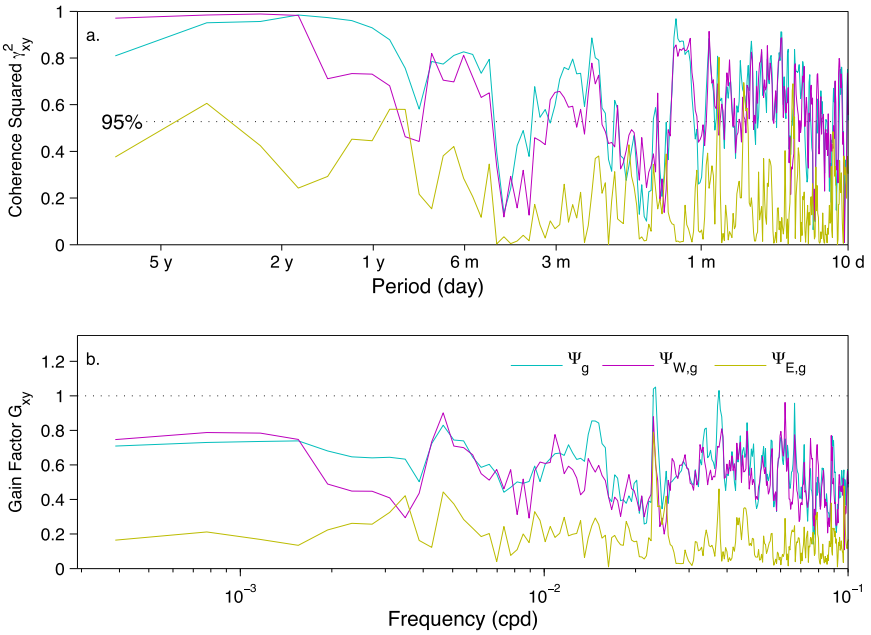

FIG. 8. (a) Multitaper coherence squared and (b) gain factor between Ψ and the various contributions to Ψ as indicated in the legend. The horizontal dotted line in (a) indicates the 95% confidence level for coherence squared, where the number of degrees of freedom is twice the number of tapers (five Slepian tapers) used for the spectral estimates. Linear trends were removed from the time series before computing the coherence squared and the gain factor. There are corresponding x axes in (a) and (b), but (a) is labeled with periods and (b) is labeled with frequencies.

cutoff lengthens. When $1/\nu_c$ = 10 days, $-T_{26}$ is most correlated with $\Psi_{W,g}$ (0.58) compared with the other contributions, and this remains approximately true down to $1/\nu_c$ = 300 days. Down to almost $1/\nu_c$ = 1000 days, $-T_{26}$ is always more correlated with $\Psi_{W,g}$ than with Ψ and Ψ_g, which is understandable because T_{26} overall is not correlated with the eastern boundary (Table 2). Because $-T_{26}$ is significantly correlated with the Ekman transport (black curve in Fig. 9, noted T_{EK}) down to $1/\nu_c$ = 2 years, $-T_{26}$ is more correlated with Ψ than with Ψ_g. Since T_{26} is a geostrophic transport, this suggests that at these time scales there exists a geostrophic adjustment or a return flow in response to the surface Ekman transport that is different from the near-instantaneous vertically uniform compensating transport imposed in the RAPID MOC calculation, and which does not enter the calculation in (5). Based on the values of $\rho_{xy}(\nu_c)$, T_{26} captures more than 50% of the variance of $\Psi_{W,g}$ at periods longer than 80 days and more than 50% of the variance of both Ψ and Ψ_g at periods longer than 230 days.

Another measure of the variability of T_{26} is its power spectrum (Fig. 7). This reveals that, depending on the frequency, T_{26} exhibits different levels of variance compared to Ψ and its contributions. Notably, the broad peak centered around the 1-year period in the Ψ spectrum, attributable to $\Psi_{E,g}$, is absent for T_{26}. A consequence is that at periods longer than approximately 8 months, the variance of T_{26} becomes less than the variance of Ψ. This is also reflected in the standard deviation of T_{26}, which becomes less than the standard deviation of Ψ when the time scales shorter than 6 months are excluded (2.6 Sv compared to 3.4 Sv; Table 1). This is potentially an advantage for capturing interannual

TABLE 2. Correlation r_{xy} matrix between the MOC time series at 26°N, the western boundary contribution, the eastern boundary contribution, the geostrophic contribution, the western and eastern boundary geostrophic contributions, and the negative of the overturning transport between 1000 and 4000 m relative to 1000 m. The upper triangle contains the correlations for the 10-day low-pass-filtered nondetrended time series and the lower triangle for the 6-month low-pass-filtered nondetrended time series. Based on a method by Ebisuzaki (1997), the values not significant at the 95% confidence level are in italics.

r_{xy}	Ψ	Ψ_g	$\Psi_{W,g}$	$\Psi_{E,g}$	$-T_{26}$
Ψ	—	0.84	0.78	*0.18*	0.44
Ψ_g	0.95	—	0.84	0.34	0.45
$\Psi_{W,g}$	0.86	0.89	—	*−0.16*	0.58
$\Psi_{E,g}$	*0.25*	*0.27*	*−0.14*	—	*−0.12*
$-T_{26}$	0.69	0.66	0.83	*−0.24*	—

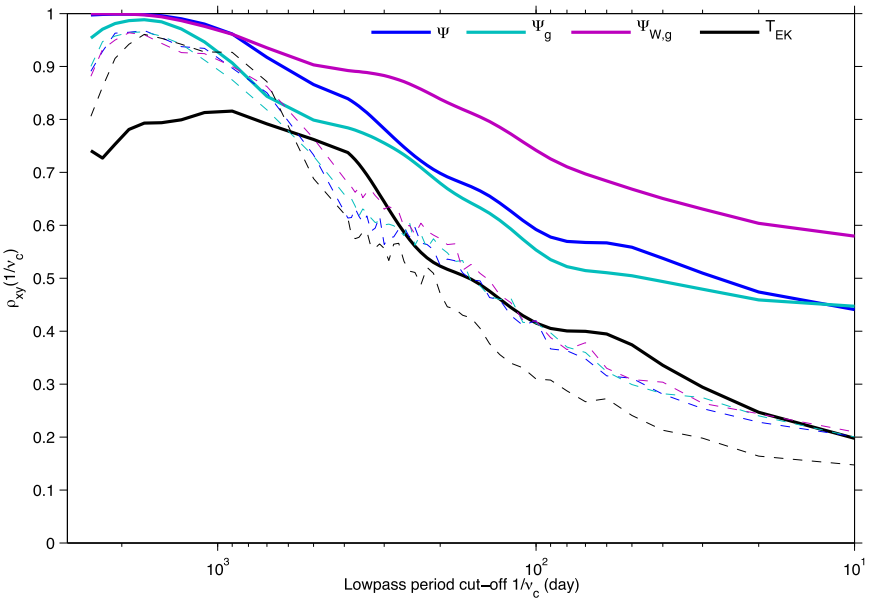

FIG. 9. Correlation as a function of the inverse of the ν_c of the low-pass filter between $-T_{26}$ and the MOC contributions as indicated in the legend. The 95% confidence level for each curve is a dashed curve of the same color.

variability as T_{26} appears shielded from the annual cycle. Similarly, power spectra of meridional transports below 1000 m from the MOVE array in the North Atlantic western ocean basin near 16°N do not display significant peaks at the annual frequency (Kanzow et al. 2008). At shorter periods, between approximately 6 months and 40 days, T_{26} exhibits more power than Ψ or any other contributions. This is also clearly seen in the time series of T_{26} compared to the MOC contributions time series (Fig. 6) or again the standard deviations for the 10-day low-pass-filtered time series (Table 1). The reason for this notable difference in variance is examined in the next subsection.

In summary, T_{26} appears to be the closest to a measure of the western geostrophic MOC. At semiannual and longer periods, it is also a measure of the geostrophic MOC and total MOC.

2) COMPARISON TO THE VERTICAL STRUCTURE OF TRANSPORT

We conduct an analysis of the geostrophic transport profile by calculating its empirical orthogonal functions (EOF). The same analysis on the total transport profile shows a dominant pattern of Ekman transport distributed in the top 100 m that is uniformly returned below. This is a construction in the solution of RAPID MOC (Kanzow et al. 2010) and is of modest interest here. To take into account different time scales of variability, we calculate the EOFs from the cumulative sum of the spectral covariance matrix (von Storch and Zwiers 2002) of the transports per unit depth up to a given frequency cutoff (note that we calculate a covariance matrix, not a correlation matrix). It is equivalent to forming covariance matrices of the transport profile after applying a low-pass filter and changing the frequency cutoff to gradually eliminate variance at short periods. For each calculation with a different cutoff frequency, the principal component (PC) time series associated with an EOF is computed by projecting that EOF on the transport profile time series after low-pass-filtering them with the same frequency cutoff. The correlations of $-T_{26}$ filtered in the same way with the PC time series and with the filtered geostrophic MOC are also calculated, assessing the significance of the correlations following Ebisuzaki (1997). The range of period cutoffs considered varies from 10 days to the length of the time series, 2578 days. Figures 10a and 10c display contour plots of the first two EOFs as a function of depths between 0 and 4000 m and as a function of the period cutoff.

The first two EOFs always explain together more than 82% of the variance, with EOF1 always explaining more than 63% of the variance (Figs. 10b,d). Overall EOF1 corresponds in its positive phase to a northward transport above approximately 1000 m, decreasing monotonically to become southward below. Yet, the vertical structure of EOF1 changes with the period cutoff. The shear of EOF1 below 1000 m is relatively weak when short periods are included, strengthening significantly when periods shorter than 100 days are excluded.

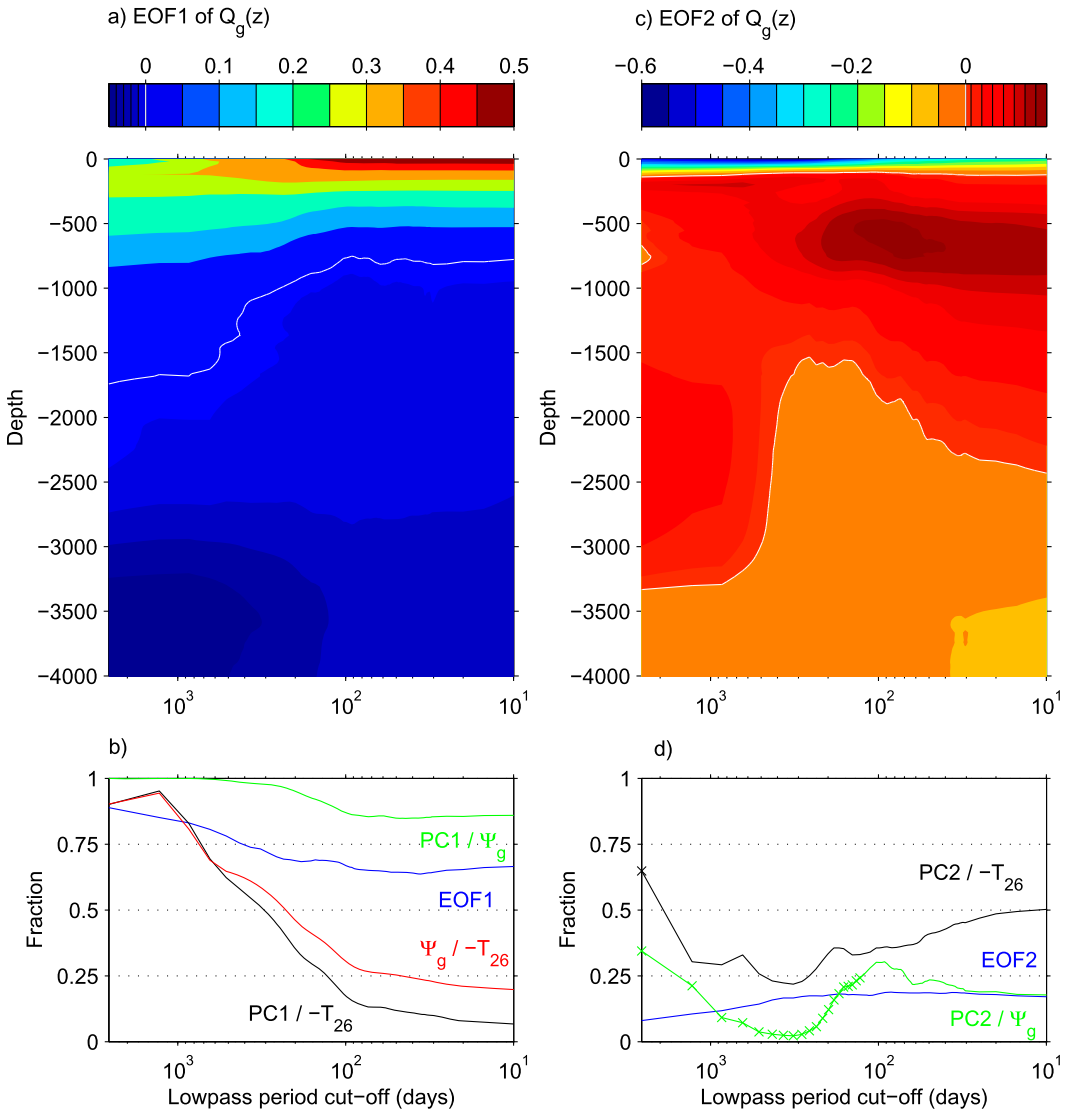

FIG. 10. Contour plots of (a) EOF1 and (c) EOF2 of the geostrophic transport profile as a function of low-pass filter period cutoff. The analysis is conducted on the full-depth transport profile but only the top 4000 m are contoured here. Fraction of variance explained by (b) EOF1 and by (d) EOF2 and correlation squared interpreted as a fraction of variance explained between the quantities as indicated by the labels. The correlation squared values that correspond to correlation values that are not significant at the 95% confidence level are indicated with cross signs on the curves.

Because T_{26} is a double depth integral of the transport shear between 1000 and 4000 m, if a mode of variability of the transport profile is vertically uniform at those depths, it is not captured by T_{26}. As such the changing shear is partly responsible for the fact that PC1 accounts for less than 6% of the variance of T_{26} with the shortest low-pass filter period cutoff, increasing to ultimately more than 90% as more short periods are excluded (Fig. 10b).

The vertical structure of EOF2 is such that in its positive phase it always corresponds to a strong southward transport in the top 150 m. Below that depth, the structure varies depending on the period cutoff. When time scales shorter than 1 year are included, EOF2 corresponds to a transport that is northward and with a local maximum near 600 m then decreases to become southward below between 1500 and 2500 m. When time scales shorter than 1 year are excluded, the vertical structure of this mode changes significantly: the subsurface northward maximum decreases and the shear below 1000 weakens. However, whatever the period cutoff, the amount of variance of Ψ_g that can be accounted for by this mode is always less than 30% (based

on significant correlation; Fig. 10d). This is understandable because EOF2 integrates to a very small transport in the top 1000 m because of its structure, which includes a zero crossing between 100 and 150 m. In fact, for a period cutoff longer than 130 days, the correlation between PC2 and Ψ_g is not significant. At the same time, the amount of variance in T_{26} that can be accounted for by EOF2 (based on the correlation squared between PC2 and T_{26}) decreases from 50% to about 25%. The dynamical nature of EOF2 at high frequency is likely due to eddies and Rossby waves impinging on the western boundary (Kanzow et al. 2009).

In summary, as more short-period variances are excluded, the variance of the geostrophic transport profile is dominantly represented by EOF1, which corresponds to a transport profile with a monotonic shear below 200 m, while the importance of a second mode, little correlated with the MOC, with variance at intermediate depth, decreases. These changes in the variability of the geostrophic transport profile and its shear explain why 1) T_{26} exhibits larger variance than Ψ_g at intermediate time scales (from 6 months approximately to 40 days), and 2) $-T_{26}$ is more strongly correlated with Ψ_g as more short-period variability is excluded. Another implication is that the maximum of the total or geostrophic streamfunction (or zero crossing of the transport profile) may well be very close to 1000 m on the time mean, yet the 1000-m level does not correspond to a node in the profile of variability, which is a function of the time scales considered. In fact, the distribution of the maximum of the streamfunction is bimodal with a deep mode centered around 1050 m and another shallower mode centered around 680 m (not shown). Filtering the time series of transports to remove time scales shorter than approximately 6 months suffices to eliminate the mode at 680 m.

A general conclusion is that the vertical structure of MOC variability depends on the time scale, being complicated at short time scales but settling to a single, simple mode at periods longer than about a year. At such long periods, T_{26} captures most of the variance of the geostrophic MOC.

4. Western transport overturnings near 41°N

In this section we assess whether the variability of the MOC near 41°N measured by Argo and altimetry data analyses as in Willis (2010) is captured by time series of meridional transports derived from OBP gradients below 1000 m on the western boundary of the North Atlantic Ocean at two sites north and south of this latitude: at 39°N from the WHOI Line W and at 42.5°N from the RAPID WAVE Line B.

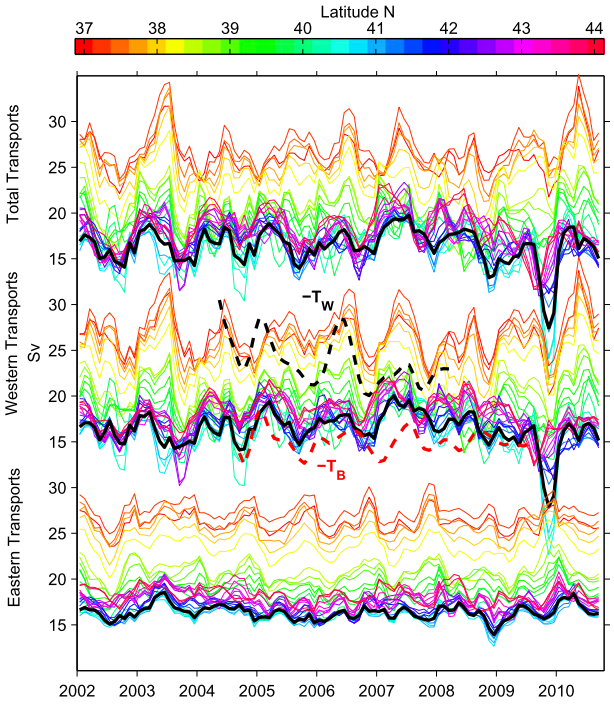

FIG. 11. Total, western, and eastern geostrophic transports in the top 1000 m for the lat range 37°–44°N in the North Atlantic from the Willis and Fu (2008) analyses of the Argo data (see text). The black curves are the averages for 40°–41.5°N. Note the changing *y* axis. Each western or eastern boundary transport is plotted as an anomaly from the mean of the total transport at the same lat. The negative of the time series of 6-month low-pass-filtered transport between 1000 and 4000 m referenced to 1000 m from WHOI Line W (black dashed) and RAPID WAVE Line B (red dashed) are plotted with arbitrary offset for comparison.

a. Geostrophic and Ekman transports between 37° and 44°N

We use the 4D Argo-based analyses of Willis and Fu (2008) between 37° and 44°N at quarter degree resolution to obtain time series of geostrophic meridional transports, as well as contributions from the western and eastern boundaries following (1). These Argo analyses are geographically bounded by the 2000-m isobaths on the west and the east of the Atlantic basin (Fig. 1), thus neglecting transports in regions shallower than 2000 m. Willis (2010) diagnosed from the Estimating the Circulation and Climate of the Ocean, phase 2 (ECCO2), model (Menemenlis 2008) that these analyses could be used between 40° and 41.5°N to obtain the basinwide geostrophic meridional transport in the top 1130 m with an rms error of only 1.1 Sv. Outside of this latitudinal band, the data miss transport over regions shallower than 2000 m and biases should be present. Nevertheless, we use these data to compute transports between 37° and 44°N, shown in Fig. 11. We compute the transports in the top 1000 m

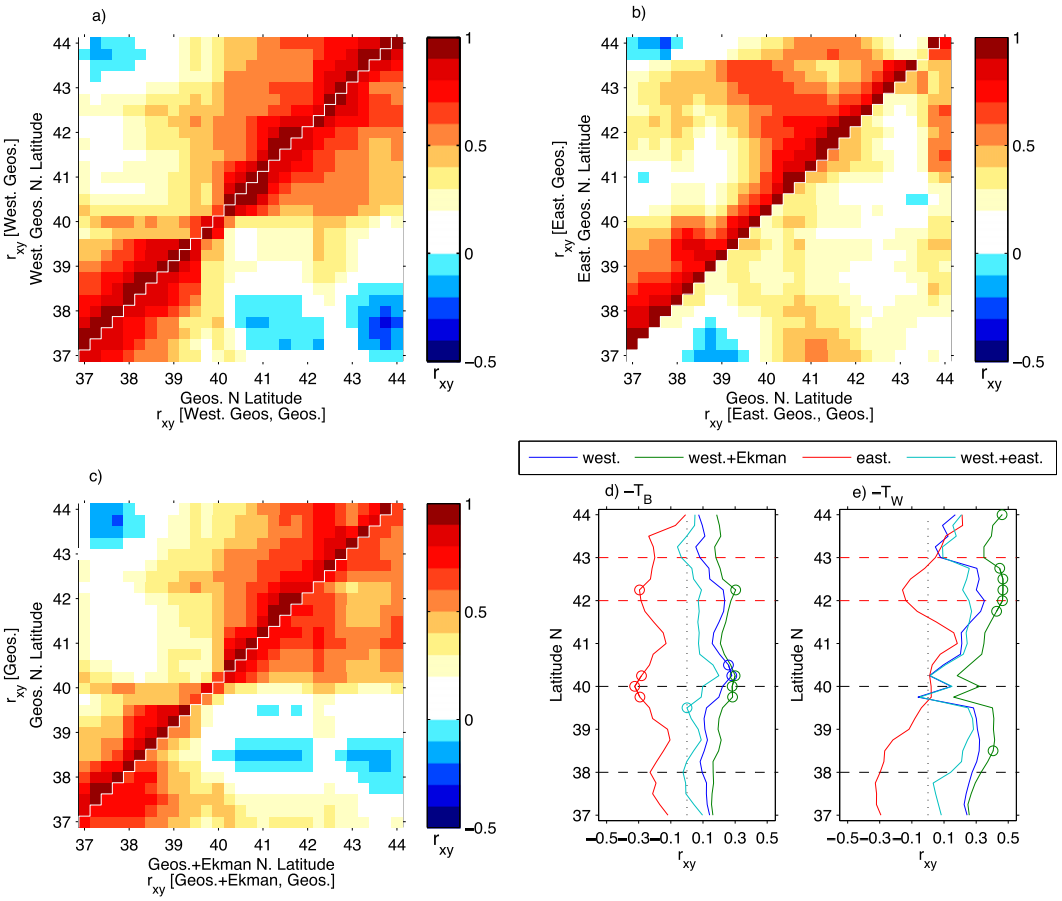

FIG. 12. Correlation r_{xy} between transports: (a) correlations between western geostrophic transports (upper triangle) and between western geostrophic and total geostrophic transports (lower triangle); (b) correlations between eastern geostrophic transports (upper triangle) and between eastern geostrophic and total geostrophic transports (lower triangle); (c) correlations between total geostrophic transports (upper triangle) and between total geostrophic and total geostrophic plus Ekman transports (lower triangle); (d) correlations between $-T_B$ and the upper-ocean transports as indicated in the legend; and (e) correlations between $-T_W$ and the upper-ocean transports as indicated in the legend. Correlations significant at the 95% confidence level in (d) and (e) are indicated by circles.

rather than the top 1130 m as in Willis (2010), in order to conduct comparisons with overturning transports relative to and below that depth, as derived in Elipot et al. (2013). The rms difference in transports at 41°N between the two choices is only 0.2 Sv. As in Willis (2010), total upper-ocean transports are obtained by adding to the geostrophic transports the Ekman transports calculated from monthly NCEP reanalyses' wind stress at approximately 1.9° latitude resolution (not shown). These Ekman transports are relatively uniform and decorrelate at most at 0.67 between 37° and 44°N.

We assess the general characteristics of the upper-ocean transports and the relative contributions from its various components by examining correlations between 37° and 44°N, shown in Fig. 12. The correlations between geostrophic, western geostrophic, eastern geostrophic, and geostrophic plus Ekman transports all show that there is a disconnection between transports north and south of 40°N, also evident in the time series themselves (Fig. 11). Such decorrelation of geostrophic transports was also seen in Bingham et al. (2007) in a coupled atmosphere–ocean model and in an ocean-only model, where 40°N corresponds roughly to the boundary between the subtropical and subpolar gyre circulations with distinct meridional transport variabilities. Correlations between western geostrophic and geostrophic transports at each latitude (diagonal of the matrix in Fig. 12a) reveal that the western contribution explains between 68% and 92% of the variance of the geostrophic transport, showing again the importance of the western boundary in this latitude range. Correlations between geostrophic and geostrophic plus Ekman transports (diagonal of the matrix in Fig. 12c) show that the geostrophic contribution explains between 17% (at 39.5°N) and 70% (at 40.5°N) of the total upper

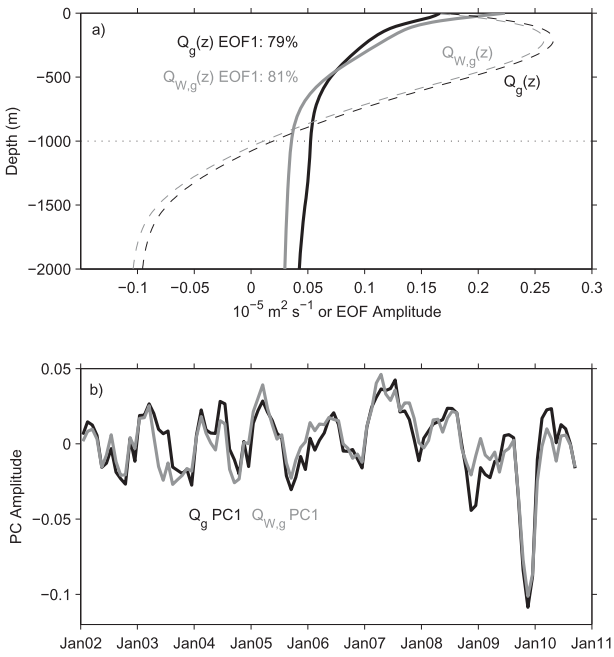

FIG. 13. EOF analyses of $Q_g(z)$ and $Q_{W,g}(z)$ profiles at 41°N: (a) EOF1 patterns; the time means of $Q_g(z)$ and $Q_{W,g}(z)$ are also plotted with dashed curves. (b) First EOFs PC time series.

transport variance. In the update of the MOC time series of Willis (2010) (Fig. 2b), the geostrophic contribution explains 64% of the total MOC variance.

EOF analyses of $Q_g(z)$ and $Q_{W,g}(z)$ averaged between 40° and 41.5°N (Fig. 13) show that the transport variability is controlled by the western boundary: EOF1 of $Q_{W,g}(z)$ and EOF1 of $Q_g(z)$ are very similar and explain both approximately 80% of the respective variances. In their positive phases they represent a northward transport anomaly that is strongly sheared in the top 500 m and near uniform below, down to 2000 m, which is in contrast to the transport variability at 26°N (Fig. 10). An analysis of the changes of the vertical structure of transport variability as a function of frequency (not shown) was conducted, but no major changes were identified as a function of period cutoff. However, because 3 months of Argo data go into each monthly transport profile, it is possible that the time resolution of the data may not be sufficient to capture the relatively high-frequency variance that is captured by RAPID MOC. The PC time series associated with EOF1 of $Q_{W,g}(z)$ and EOF1 of $Q_g(z)$ explain almost all the variance of their respective top 1000-m layer transport (correlations are 0.99). Most remarkable, the correlation between the top 1000-m layer total transport and PC1 of $Q_{W,g}(z)$ is 0.92, which shows that EOF1 of $Q_{W,g}(z)$ is the dominant mode of variability of the geostrophic MOC at 41°N.

b. Comparisons to overturning transports from OBP

Is the MOC time series near 41°N from Willis (2010) captured by OBP gradient on the western boundary? To answer this question we compare the upper-ocean transports between 37° and 44°N to deep overturning transports as derived at 26°N; that is,

$$T = \int_{z_1}^{z_2} \frac{-p'_W(z)}{\rho_0 f} dz. \tag{6}$$

The first estimate of (6) that we consider is T_B (Fig. 2a), derived by Elipot et al. (2013) where p'_W was estimated from OBP gradients between 1000 and 4000 m, calculated from BPR data from the RAPID WAVE Line B spanning the continental slope between 42° and 43°N (Fig. 1). Here T_B is augmented by 1 year of BPR data from the first deployment of the RAPID–Scotian (RS) Line, successor of Line B through the continuation of RAPID WAVE under the RAPID–Will the Atlantic Thermohaline Circulation Halt? (WATCH) program (Hughes et al. 2013). At time scales longer than 1 year, T_B is unreliable because of finite deployment times and BPR drift correction. The second estimate of (6) is T_W (Fig. 2c), derived by Elipot et al. (2013) where p'_W was estimated between 1000 and 4120 m, following the methodology of Hughes et al. (2013), using data from the WHOI Line W array located on the continental slope between 38° and 40°N (Fig. 1). Because T_W is not estimated from BPR data, this time series should not suffer from drift corrections or discontinuities like T_B, as explained in Hughes et al. (2013). For comparisons of the upper-ocean transports, we actually consider monthly averages of $-T_B$ and $-T_W$ centered on the middle date of each month. This leaves time series of only 62 points for $-T_B$ and 42 points for $-T_W$.

We examine the correlations of $-T_B$ and $-T_W$ as a function of latitude with the upper-ocean geostrophic transports, their eastern and western contributions, and their western contributions augmented by Ekman transports (Figs. 12d,e). The transports $-T_B$ and $-T_W$ are not significantly correlated with the upper-ocean geostrophic transports. The transport $-T_B$ is significantly negatively correlated with the eastern geostrophic transports around 40°N, but this correlation should not be very relevant considering the low values of eastern transports (Fig. 11). Both transports $-T_B$ and $-T_W$ are generally positively correlated with the western geostrophic transports, but this correlation is significant only for $-T_B$ at 40.25°–40.5°N. When the Ekman transports are added to the western geostrophic transports, the correlations become stronger (reaching 0.3 for $-T_B$ and 0.45 for $-T_W$) and more often significant in a number of latitude bands: for

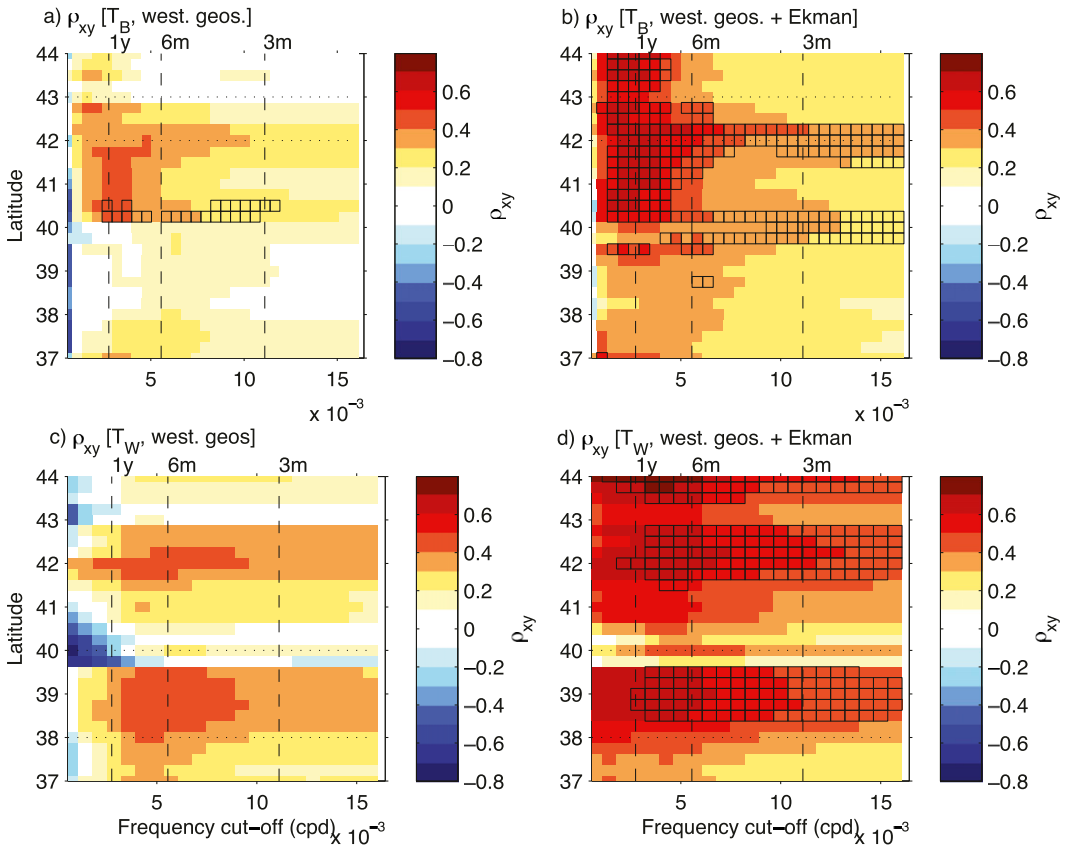

FIG. 14. Cumulative integral of normalized cospectra as a function of frequency cutoff between (a),(b) $-T_B$ or (c),(d) $-T_W$ and the (left) western geostrophic or (right) western geostrophic plus Ekman geostrophic. The black squares delineate the values that are significant at the 95% confidence level. The vertical dashed lines indicate the 1-yr, 6-month, and 3-month periods. The dotted horizontal lines in (a) and (b) indicate the range of lat of RAPID WAVE Line B and in (c) and (d) indicate the range of lat of WHOI Line W.

$-T_B$ around 40° and at 42.25° and for $-T_W$ at 38.5°, between 41.75° and 42.75°, and at 44°N. Thus, based on these correlation results, both T_B and T_W capture modest amounts of the variance of the western plus Ekman contributions to the upper-ocean transports, but within different latitudes.

We are limited by the number of points in our monthly time series for a thorough analysis in the spectral domain as we conducted at 26°N. Nevertheless, Fig. 14 shows the equivalent[1] of the quantity ρ_{xy} introduced earlier, between $-T_B$ and $-T_W$ on one hand and the western geostrophic and western geostrophic plus Ekman transports on the other hand. As previously, we use the method of Ebisuzaki (1997) to assess the significance of the calculation at the 95% confidence level. Both $-T_B$ and $-T_W$ exhibit positive ρ_{xy} values with the western geostrophic transports (Figs. 14a,c) throughout most latitudes, but $-T_W$ exhibits large negative ρ_{xy} values around 40°N. However, the east–west orientation of the 2000-m isobath near 40°N may render the Argo sampling problematic there. The $-T_B$ term exhibits larger ρ_{xy} values with the western transports between 40° and 43°N, while $-T_W$ exhibits larger ρ_{xy} values between 37.75° and 39.5°N. Thus, 40°N is a clear separation of the frequency–latitude space of correlation. This is understandable if one takes into account the decrease of correlation between the upper-ocean transports north and south of 40°N (Fig. 12) and the latitudes of the Line B and Line W arrays. Values of ρ_{xy} with the western geostrophic transports are greater than 0.45 near-annual time scales for $-T_B$ and from 3-month and longer time scales for $-T_W$. However, only $-T_B$ exhibits significant values of ρ_{xy} at 40.25°–40.5°N. By augmenting the western geostrophic transports with the Ekman transports, the values of ρ_{xy} and their significance increase dramatically (Figs. 14b,d). In those cases, ρ_{xy} for $-T_B$ now exceeds 0.6 when periods shorter than 6 months

[1] The cumulative integral of the cospectrum divided by the square root of the product of the autospectra.

are excluded from the computation at 42.25°N. This is also the case for $-T_W$ but in broader latitude bands, from 38.25° to 39.5°N and from 41.5° to 42.75°N. In addition, ρ_{xy} for $-T_W$ reaches values greater than 0.7 from the 6-month period near 44°N. Overall, the conclusion is that T_B captures a modest yet nonnegligible fraction (at least 20%) of the variance of the western geostrophic transports for near-annual periods and a larger fraction (up to 47%) of the variance of the western geostrophic plus Ekman transports north of 40°N for semiannual and longer periods. Similarly, T_W captures a slightly greater fraction (up to 25%) of the western geostrophic transports for semiannual and longer periods and a larger fraction of the variance of the western geostrophic plus Ekman transports north of 40°N for semiannual and longer periods (up to 60% at 44°N, but only up to 47% at lower latitudes). In Fig. 11, the linear relationships between OBP gradient-derived transports and Argo transports are visually evident when 6-month low-pass-filtered versions of T_W and T_B are plotted alongside the Argo transports.

In summary, it has been shown that transports relative to and below 1000 m from OBP gradients near 41°N are capturing some of the variance of the geostrophic MOC because they are anticorrelated with upper-ocean western geostrophic transports for approximately semiannual and longer time scales. In addition, this anticorrelation is stronger with upper-ocean western geostrophic transports augmented by Ekman transports. Because T_B and T_W are geostrophic transports by construction, this suggests that there exist a geostrophic adjustment or return flow in response to the upper-ocean Ekman transport, similar to what we showed at 26°N. Yet, the amount of variance shared by the upper and lower transports is not as strong as the one obtained from the 26°N analysis, but the results are nevertheless consistent between the two latitudes. It is possible that the transport missed by the Argo floats over regions onshore of the 2000-m isobath on the west within the latitudes of Line B and Line W is sufficient to lower the correlation between the upper-ocean transports and the lower return transports captured by OBP gradients.

5. Coherence of overturnings between 26° and 41°N

We now have at our disposal for comparisons two time series of the top 1000-m integrated geostrophic and total transports at 26° and 41°N and three time series of overturning transport relative to and below 1000 m (Fig. 2).

a. Coherence of MOC time series at 26° and 41°N

The spectra of Ψ at 26° and 41°N (Fig. 15a) both have their maximum power near the annual period, but also some power toward longer periods. The 26°N Ψ additionally exhibits relatively high power near the semiannual period, but not so much the 41°N Ψ. At 26°N, the spectrum of Ψ_g is relatively elevated at the near-annual period, but that it is less the case for the spectrum of $\Psi_{W,g}$, once again demonstrating the importance of the eastern boundary at that time scale (Kanzow et al. 2010). This seems to be also the case at 41°N where the near-annual period dominates the spectrum of Ψ_g, but not the spectrum of $\Psi_{W,g}$.

How much of the MOC variance is coherent as a function of latitude? The cross-spectrum between Ψ at 26° and 41°N (not shown) has a peak near the annual period, as well as the cross-spectrum of Ψ_g, albeit less pronounced. In Fig. 15b, significant coherence squared between Ψ at 26° and 41°N is found at periods between 8 and 12 months. Between Ψ_g, significant coherence squared is found at the 9-month period and at periods near 3–4 months, but the autospectra of the Ψ_g are very low at these last periods. In Fig. 15c the coherence phase between the Ψ at near-annual periods is between $-90°$ and $-135°$, which implies that the 41°N Ψ precedes the 26°N Ψ by approximately a quarter of a cycle at these time scales (or 3 months on the annual time scale). The coherence phase between the Ψ_g at near-annual periods is between $-96°$ and $-160°$. Overall, at periods where the Ψ time series or the Ψ_g time series seem to covary, their phases are close to being in quadrature or 90° apart. As a consequence, the correlations of the time series are zero. This is a consequence of the specific phase arrangement, rather than indicating that the two time series are unrelated. Mielke et al. (2013) came to a similar conclusion by analyzing the seasonal cycle of the MOC at 26° and 41°N defined by monthly averages. They found that the MOC seasonal cycles at the two latitudes were apart by approximately 90° (their Fig. 1c). They also found that the geostrophic MOC (which they called MOC minus Ekman) had opposing phases; that is, they were 180° apart, whereas we find here that this phase difference is somewhat smaller, between $-96°$ and $-160°$.

The cross-spectrum of $\Psi_{W,g}$ at 26° and 41°N (not shown) has low amplitudes, and the coherence squared is little significant, except at the longest periods where the coherence phase is near zero (Figs. 15b,c). This interannual coherent covariance of $\Psi_{W,g}$ at these two latitudes may reflect the extreme event of winter 2009–10. In November 2009, the total geostrophic transport near 41°N reached an unprecedented low value due to the western geostrophic transport (Fig. 11). The Ekman transport further amplified this minimum for the total MOC at 41°N (Fig. 2b). The MOC at 26°N also reached a minimum about 1 month later (Fig. 2d), which was the combination of a relatively strong southward

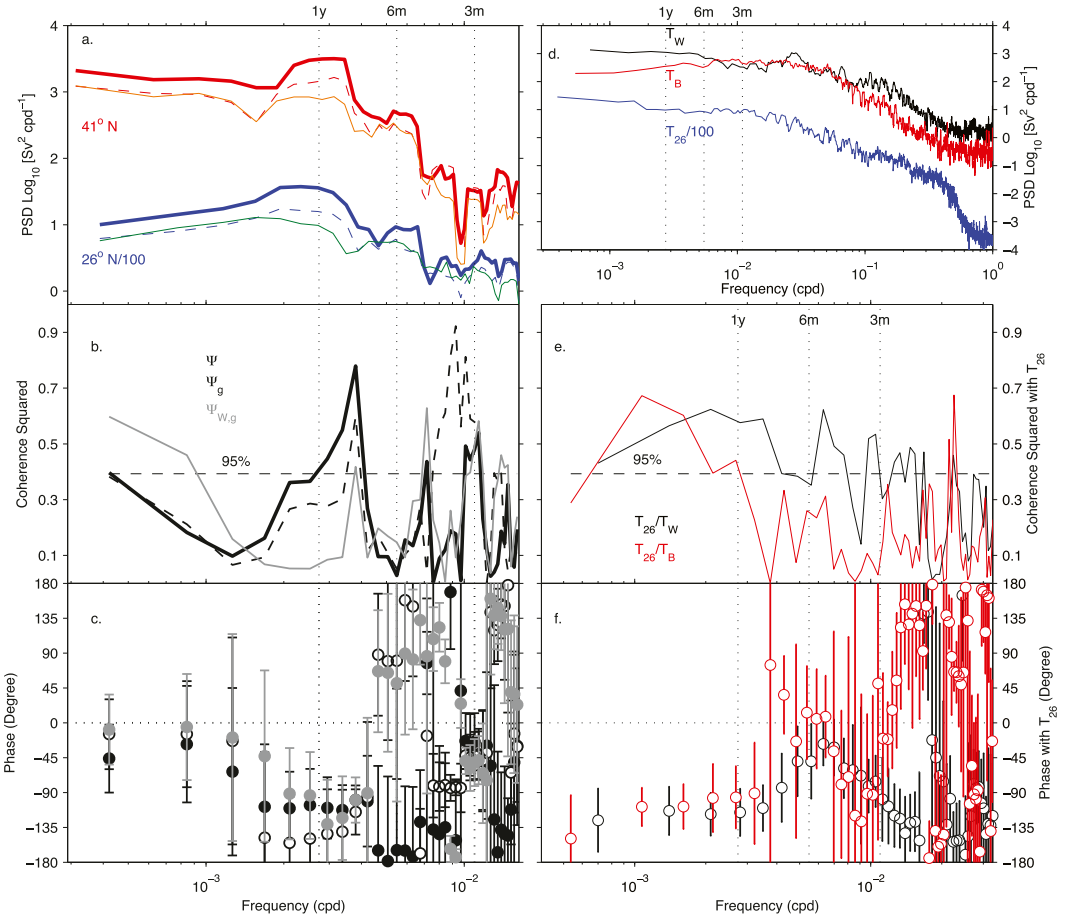

FIG. 15. (a) Power spectral density of MOC time series at 41° and 26°N. Total MOC are heavy lines, geostrophic MOC are dashed lines, western geostrophic are thin lines, following the legends of Figs. 2b and 2d. The spectra for 26°N are offset by −2 decades. (b) Coherence squared and (c) coherence phase between Ψ [heavy black line in (b) and filled black symbols in (c)], Ψ_g [dashed black line in (b) and open black symbols in (c)], and $\Psi_{W,g}$ [gray line in (b) and gray symbols in (c)] at 41° and 26°N. (d) Power spectral density of T_W (black) and T_B (red) and T_{26} (blue) offset by −2 decades. (e) Coherence squared and (f) coherence phase between T_B and T_{26} (red) and between T_W and T_{26} (black). Error bars for phase estimates are 95% confidence intervals. Spectral quantities are estimated using a multitaper estimator with five Slepian tapers following Percival and Walden (1993).

upper-midocean transport, a weakening of the deep return flow (3000–5000 m) that may be attributed to the thermocline depth changes at the western boundary, and a strong southward Ekman transport (McCarthy et al. 2012). This suggests that this extreme event was large scale and due to the geostrophic variability on the western boundary, both at 26° and 41°N. Yet, at periods between 6 months and 1 year, despite the relative low coherence squared of the $\Psi_{W,g}$, the coherence phase is near −90° (Figs. 15b,c). The correlation between the two $\Psi_{W,g}$ time series is 0.30 because of the low-frequency in-phase relationship, but the associated p value is 0.17, making it insignificant.

In summary, the coherence between latitudes of the geostrophic overturning transports and western boundary contributions is weak. Nevertheless, there is an indication that these geostrophic transports are in near quadrature at the annual period.

b. *Coherence of deep overturning transports at 26°, 39°, and 42.5°N*

The outstanding question now is: do time series of overturning transports relative to and below 1000 m capture the same covariance and phase as the MOC time series? Pairwise coherence squared and coherence phase between T_{26}, T_W, and T_B are shown in Figs. 15e and 15f, respectively. While T_W has a relatively high coherence squared with T_{26} for periods longer than 2 months, T_B is significantly coherent with T_{26} only for periods longer than 15 months. This result for T_B is less reliable because at such time scales the variance is likely to have been

altered by the detrending of BPR records. However, in both cases the coherence phases are near −90°. As a consequence, the correlations between T_{26} on one hand and T_B and T_W on the other hand are zero despite significant covariances. Attempts to identify significant time delays as in Elipot et al. (2013) from T_W and T_B to T_{26}, which could have been indicative of the southward propagation of coastally trapped boundary waves, were unsuccessful. The analysis of an OGCM by van Sebille et al. (2011) suggests that the advection time scale based on lag correlation of salinity of Labrador Sea Water between 26°N and 39°–42.5°N is longer than 2 years, a result that cannot explain the observed phases in Fig. 15d.

In conclusion, the time series of western contribution to transport relative to and below 1000 m exhibit the same approximate 90° out-of-phase, or near quadrature, relationship as the one observed between the conventional MOC time series at 41° and 26°N, albeit more strongly. The dynamics behind this relationship will be investigated elsewhere. For this paper, the conclusion is that the small part of the MOC signal that is coherent between 41° and 26°N is also captured by deep overturning transports on the western boundary of the North Atlantic Ocean.

6. Summary and remarks

This study, based mainly on the five time series (and their variants) shown in Fig. 2, leads to the following conclusions:

- The MOC time series at 26° and 41°N are coherent on near-annual time scales. The phase associated with this coherence is close to 90°, with 41° leading 26°N, resulting in a nonsignificant correlation (Fig. 15).
- The dominant signal of the MOC at both latitudes is the geostrophic contribution (Figs. 2, 8, and 12), which is in turn dominated by the western boundary contribution (Figs. 6, 12, and 13; Table 2). At 26°N, the western geostrophic MOC explains 60% of the total MOC variance for time scales longer than 10 days and 74% of the total variance for time scales longer than 6 months. At 41°N, based on analyses of monthly transports, the western boundary geostrophic MOC explains 84% of the geostrophic MOC variance and 51% of the variance of the total MOC that includes the Ekman transport.
- The time series at 26° and 41°N of geostrophic and of western geostrophic contributions to the MOC show less coherence between latitudes than the total MOC time series do, but nevertheless exhibit the same phase relationship close to 90° on near-annual time scales, with 41° leading 26°N (Fig. 15). At interannual time scales these time series are approximately in phase, as evidenced by the strong downturn event of winter 2009–10 (Fig. 2).
- At 26°N, the western boundary contribution to the geostrophic transport in the 1000–4000-m layer, relative to 1000 m, called here T_{26}, captures more than 50% of the variance of both the MOC and its geostrophic contribution at periods longer than 230 days (Fig. 9), but not at shorter periods. This is because at periods substantially shorter than a year, different vertical structures of the transport profile make important contributions to the MOC variability (Fig. 10). However, at longer periods the variability settles down to a single mode, which is well captured by the transport shear on the western boundary only.
- With limitations on the time scales that can be investigated, it is shown with 1 year of BPR records that T_{26} can also be estimated by integrating with depth the OBP gradient on the western boundary, instead of using RAPID MOC data (Fig. 5).
- Near 41°N, two OBP gradient time series on the western boundary integrated with depth to form western geostrophic transports in the 1000–4000-m layer relative to 1000 m, called here T_W and T_B, capture a modest but significant fraction (20%–25%) of the geostrophic MOC on near-annual time scales. On semiannual and longer time scales, T_W and T_B capture a larger fraction (approximately 47%) of the total MOC (Figs. 12, 14).
- The phase relationship at near-annual periods between T_{26} and either T_B or T_W is the same as the upper-ocean geostrophic MOC time series, with 41° leading 26°N by approximately 90° (Fig. 15).

The ability of OBP gradients to capture the geostrophic MOC on the western boundary from semiannual time scales is fortunate for observational purposes because it is the dominant signal of the MOC. Taken together, the conclusions above suggest that OBP gradient observations along the western boundary of the North Atlantic can be used to monitor the MOC and its meridionally coherent variability. One obstacle is that OBP cannot be measured reliably at long or climate time scales from BPRs because of the limitation on the technology of pressure sensors found on BPRs. Fortunately, it is not the boundary OBP itself but the boundary OBP gradient that is relevant because it is proportional to overturning, or vertically sheared, meridional transports according to geostrophy. The method of Hughes et al. (2013) aims to calculate OBP gradients in steps along a boundary with respect to an approximate 1000-m reference level, using relatively inexpensive arrays of short moorings deployed along the continental slope to measure near-bottom

geostrophic velocity and density. They showed that the error for their so-called stepping method at the RAPID WAVE Scotian Line at 42.5°N leads to a transport error of less than 1 Sv for the zonally integrated flow between 1100 and 3900 m. Elipot et al. (2013) applied this method to estimate a time series of western transport relative to and below 1000 m at the WHOI Line W mooring array near 39°N (Toole et al. 2011) and applied another method based on BPR data to estimate the same transport quantity from the RAPID WAVE array Line B near 42.5°N. The transport estimates of Elipot et al. (2013) were derived from observational arrays that were not designed, and therefore not optimal, for the purpose of estimating boundary contribution to zonally integrated meridional transport. Conceptually, the approach of measuring the deep western boundary variability by integrating the western transport shear from a fixed reference level converges with the approach taken at the MOVE array near 16°N since 2000, which is to observe the southward return flow in the western half of the North Atlantic basin using the geostrophic transports' reference to a fixed level (Send et al. 2011). At the MOVE array, however, 1000 m is a less adequate reference level and Send et al. (2011) find that a 4950-m reference level (at the interface between North Atlantic Deep Water and Antarctic Bottom Water masses) is more appropriate to capture long-term variability of transports. Nevertheless, our study showed, with the help of RAPID MOC data, that the western boundary contribution to meridional transport below and relative to 1000 m is indeed representative of the North Atlantic MOC at 26°N. We also showed that the time series of OBP-derived transport derived by Elipot et al. (2013) near 41°N capture significant variability of western boundary overturning processes. The continuation of the RAPID WAVE array program for the time period 2008–14 (Hughes et al. 2013) aims to obtain western overturning transports from an array specifically designed for that purpose.

Acknowledgments. This work was supported by the U.K. Natural Environment Research Council as part of the RAPID program. Part of this work was carried out at the Jet Propulsion Laboratory, California Institute of Technology, under a contract with the National Aeronautics and Space Administration. Thanks to Miguel Ángel Morales Maqueda for supervising the deployment and recovery of the data. Conversations with Ric Williams and Sofia Olhede were helpful in the development of this work. Data from the RAPID–MOCHA program are funded by the U.S. National Science Foundation and U.K. Natural Environment Research Council (and are freely available at http://www.rapid.ac.uk/rapidmoc/ and www.rsmas.miami.edu/users/mocha).

REFERENCES

Baringer, M., and J. Larsen, 2001: Sixteen years of Florida Current transport at 27°N. *Geophys. Res. Lett.,* **28** (16), 3179–3182.

Bendat, J. S., and A. G. Piersol, 1986: *Random Data: Analysis and Measurements Procedures.* 3rd ed. John Wiley & Sons, 594 pp.

Bingham, R., and C. Hughes, 2008: Determining North Atlantic meridional transport variability from pressure on the western boundary: A model investigation. *J. Geophys. Res.,* **113,** C09008, doi:10.1029/2007JC004679.

——, ——, V. Roussenov, and R. Williams, 2007: Meridional coherence of the North Atlantic meridional overturning circulation. *Geophys. Res. Lett.,* **34,** L23606, doi:10.1029/2007GL031731.

Bower, A., M. Lozier, S. Gary, and C. Böning, 2009: Interior pathways of the North Atlantic meridional overturning circulation. *Nature,* **459,** 243–247.

Chidichimo, M., T. Kanzow, S. Cunningham, W. Johns, and J. Marotzke, 2010: The contribution of eastern-boundary density variations to the Atlantic meridional overturning circulation at 26.5°N. *Ocean Sci.,* **6,** 475–490.

Ebisuzaki, W., 1997: A method to estimate the statistical significance of a correlation when the data are serially correlated. *J. Climate,* **10,** 2147–2153.

Elipot, S., C. W. Hughes, S. Olhede, and J. Toole, 2013: Coherence of western boundary pressure at the RAPID WAVE array: Boundary wave adjustments or deep western boundary current advection? *J. Phys. Oceanogr.,* **43,** 744–765.

Hughes, C. W., S. Elipot, M. A. Morales Maqueda, and J. Loder, 2013: Test of a method for monitoring the geostrophic meridional overturning circulation using only boundary measurements. *J. Atmos. Oceanic Technol.,* **30,** 789–809.

Huthnance, J., 1978: On coastal trapped waves: Analysis and numerical calculation by inverse iteration. *J. Phys. Oceanogr.,* **8,** 74–92.

Johns, W. E., L. M. Beal, M. O. Baringer, J. R. Molina, S. A. Cunningham, T. Kanzow, and D. Rayner, 2008: Variability of shallow and deep western boundary currents off the Bahamas during 2004–05: Results from the 26°N RAPID–MOC array. *J. Phys. Oceanogr.,* **38,** 605–623.

——, and Coauthors, 2011: Continuous, array-based estimates of Atlantic Ocean heat transport at 26.5°N. *J. Climate,* **24,** 2429–2449.

Johnson, H., and D. Marshall, 2002: A theory for the surface Atlantic response to thermohaline variability. *J. Phys. Oceanogr.,* **32,** 1121–1132.

Kanzow, T., and Coauthors, 2007: Observed flow compensation associated with the MOC at 26.5°N in the Atlantic. *Science,* **317,** 938–941.

——, U. Send, and M. McCartney, 2008: On the variability of the deep meridional transports in the tropical North Atlantic. *Deep-Sea Res.,* **55,** 1601–1623, doi:10.1016/j.dsr.2008.07.011.

——, H. L. Johnson, D. P. Marshall, S. A. Cunningham, J. J.-M. Hirschi, A. Mujahid, H. L. Bryden, and W. E. Johns, 2009: Basinwide integrated volume transports in an eddy-filled ocean. *J. Phys. Oceanogr.,* **39,** 3091–3110.

——, and Coauthors, 2010: Seasonal variability of the Atlantic meridional overturning circulation at 26.5°N. *J. Climate,* **23,** 5678–5698.

McCarthy, G., and Coauthors, 2012: Observed interannual variability of the Atlantic meridional overturning circulation

at 26.5°N. *Geophys. Res. Lett.,* **39,** L19609, doi:10.1029/2012GL052933.

Meinen, C. S., W. E. Johns, S. L. Garzoli, E. van Sebille, D. Rayner, T. Kanzow, and M. O. Baringer, 2012: Variability of the deep western boundary current at 26.5°N during 2004–2009. *Deep-Sea Res. II,* **85,** 154–168.

Menemenlis, D. A., 2008: ECCO2: High resolution global ocean and sea ice data synthesis. *Mercator Ocean Quarterly Newsletter,* No. 31, Mercator Ocean, Ramonville Saint-Agne, France, 13–21.

Mielke, C., E. Frajka-Williams, and J. Baehr, 2013: Observed and simulated variability of the AMOC at 26°N and 41°N. *Geophys. Res. Lett.,* **40,** 1159–1164, doi:10.1002/grl.50233.

Percival, D. B., and A. T. Walden, 1993: *Spectral Analysis for Physical Applications.* Cambridge University Press, 612 pp.

Polster, A., M. Fabian, and H. Villinger, 2009: Effective resolution and drift of Paroscientific pressure sensors derived from long-term seafloor measurements. *Geochem. Geophys. Geosyst.,* **10,** Q08008, doi:10.1029/2009GC002532.

Rayner, D., and Coauthors, 2011: Monitoring the Atlantic meridional overturning circulation. *Deep-Sea Res.,* **58,** 1744–1753, doi:10.1016/j.dsr2.2010.10.056.

Roussenov, V., R. Williams, C. Hughes, and R. Bingham, 2008: Boundary wave communication of bottom pressure and overturning changes for the North Atlantic. *J. Geophys. Res.,* **113,** C08042, doi:10.1029/2007JC004501.

Send, U., M. Lankhorst, and T. Kanzow, 2011: Observation of decadal change in the Atlantic meridional overturning circulation using 10 years of continuous transport data. *Geophys. Res. Lett.,* **38,** L24606, doi:10.1029/2011GL049801.

Smith, W. H. F., and D. T. Sandwell, 1997: Global sea floor topography from satellite altimetry and ship depth soundings. *Science,* **277,** 1956–1962.

Stommel, H. M., 1958: The abyssal circulation. *Deep-Sea Res.,* **5,** 80–82.

Toole, J., R. Curry, T. Joyce, M. McCartney, and B. Penã Molino, 2011: Transport of the North Atlantic deep western boundary current about 39°N, 70°W: 2004–2008. *Deep-Sea Res. II,* **58,** 1768–1780, doi:10.1016/j.dsr2.2010.10.058.

van Sebille, E., M. Baringer, W. Johns, C. Meinen, L. Beal, M. de Jong, and H. van Aken, 2011: Propagation pathways of classical Labrador Sea water from its source region to 26°N. *J. Geophys. Res.,* **116,** C12027, doi:10.1029/2011JC007171.

von Storch, H., and F. Zwiers, 2002: *Statistical Analysis in Climate Research.* Cambridge University Press, 496 pp.

Willis, J., 2010: Can in situ floats and satellite altimeters detect long-term changes in Atlantic Ocean overturning. *Geophys. Res. Lett.,* **37,** L06602, doi:10.1029/2010GL042372.

——, and L. Fu, 2008: Combining altimeter and subsurface float data to estimate the time-averaged circulation in the upper ocean. *J. Geophys. Res.,* **113,** C12017, doi:10.1029/2007JC004690.

Zhang, R., 2010: Latitudinal dependence of Atlantic meridional overturning circulation (AMOC) variations. *Geophys. Res. Lett.,* **37,** L16703, doi:10.1029/2010GL044474.